JOURNAL OF GEOPHYSICAL RESEARCH, VOL. 111, E11005, doi:10.1029/2004JE002379, 2006

Internal structure of Rhea

Julie Castillo-Rogez[1]

Received 5 November 2004; revised 26 June 2006; accepted 5 July 2006; published 17 November 2006.

[1] We model the interior of Rhea on the basis of observational constraints and the results from geodynamical models available in the literature. Ten main types of models are defined, depending on the presence or absence of a high-pressure ice layer (ice II), and the extent of separation of the rock component from the volatiles. The degree-two gravity coefficients are computed for each of these models in order to assess which properties of the interior are likely to be inferred from *Cassini* radio science measurements scheduled on 26 November 2005. C_{22} greater than 2.5×10^{-4} indicates that the satellite is undifferentiated, except for a slight increase in density with depth resulting from material self-compression. C_{22} between 1.67×10^{-4} (lower bound) and 1.90×10^{-4} indicates the presence of a rocky core, whose radius can be determined from the satellite's mass and ices densities, for a given temperature profile. For other values, most of the ten models cannot be distinguished from each other. However, assumptions on the density of the rock phase, presence or absence of ice II, and the degree of differentiation could allow a unique model to be determined in many cases. While the calculation presented in this work assumes that Rhea is in hydrostatic equilibrium, it is likely that Rhea' gravity field is partly affected by nonhydrostatic anomalies.

Citation: Castillo-Rogez, J. (2006), Internal structure of Rhea, *J. Geophys. Res.*, *111*, E11005, doi:10.1029/2004JE002379.

1. Introduction

[2] In the early 1980s, the deep space missions Voyager I and II provided crucial constraints on the properties of the Saturnian satellites. Rhea is a medium-sized icy satellite. Photogeology shows no recent geological activity expressed at its surface [*Morrison et al.*, 1986]. Owing to the high crater density and little resurfacing (especially for craters smaller than 30 km in diameter), Rhea is often compared to Callisto as a "dead" body. Models of geodynamical evolution usually agree that medium-sized satellites did not have enough accretional and radiogenic energy for full differentiation of the interior [e.g., *McKinnon*, 1998]. However, some studies [e.g., *Consolmagno*, 1985] consider models that differentiated enough to separate a rocky core from an icy mantle. Thus accurate information on the internal structure of the Saturnian satellites can bring crucial information on the conditions in which the satellites formed and evolved.

[3] To obtain more information about a planetary body's internal structure it is necessary to measure the low degree components of the gravity field, which provide information on the mass and the dimensionless moment of inertia. These two parameters allow us to study the composition and the degree of differentiation of a body, which are crucial constraints on models of thermal evolution [e.g., *Lupo and Lewis*, 1979; *Consolmagno*, 1985]. These models, in turn, can be related to the surface morphology seen by the spacecraft instruments.

[4] The Cassini-Huygens mission will greatly improve our knowledge of the interior of Rhea. During Cassini's tour, targeted flybys are dedicated to the measurement of the gravity fields of Rhea, Titan and Saturn, and of the mass of Saturn's major satellites, by means of two-way Doppler tracking. Cassini is equipped with radio science subsystems with the capability to receive two-way X- and Ka-band signals. New instrumentation and the availability of the Ka-band downlink permit the determination of the spacecraft velocity with an accuracy at least ten times better than for the Voyager spacecraft. Details about the science objectives at Saturn's satellites and the instruments onboard Cassini are summarized by *Lunine and Soderblom* [2002] and *Matson et al.* [2002].

[5] The closest flyby of Rhea by Cassini occurred on 26 November 2005. Determining Rhea's gravity field from Cassini radio science measurements is the topic of an article published by *Anderson et al.* [2003]. That paper focuses only on models differentiated into a rocky core and an icy mantle. The purpose of the present study is to explore a larger range of Rhea models and assess the ability of the Cassini-Huygens data to discriminate among various possibilities for the satellite's internal structure. In particular, we take into account the transition of ice I into ice II. This transition is expected to take place between 350 km and 450 km depth, as a function of the temperature profile. The density increase of 20% due to ice II must not be neglected in order to produce realistic gravity field models. Hence we consider a much broader range of models than *Anderson et al.* [2003].

[6] In the next part of the paper we present the different models of Rhea's interior. These are designed to be consistent with the observational constraints and the available

[1]Jet Propulsion Laboratory, California Institute of Technology, Pasadena, California, USA.

Table 1. Dates and Distances of Rhea Encounters

Flyby Characteristics	Pioneer	Voyager I	Voyager II	*Cassini* Flyby
Date of closest approach (UTC)	1 September 1979 at 22:30	13 November 1980 at 06:11	26 August 1981 at 06:30	26 November 2005 at 22:35:52
Distance at closest approach, km	346,000	74,000	646,000	1500

numerical models for the geodynamical and thermal evolution of this satellite. Section 3 presents the values of the degree-two, gravity coefficients corresponding to the different models. Application of these results to the analysis of upcoming measurements of Rhea's gravity field is presented in section 4. We discuss these results in terms of the uncertainties to be expected on the measurements, and we consider also to what extent these data constrain model parameters. Section 5 summarizes the main results.

2. Modeling of Rhea's Interior

[7] Models of Rhea are constrained by the values of mass and mean radius provided by the *Cassini* mission. We also extensively draw upon the numerous studies published in the early eighties focusing on dynamical evolution modeling and comparisons between the satellites of the Saturnian system.

2.1. Observational Constraints

[8] Voyager I flew by Rhea on 12 November 1980. Characteristics of this encounter are compared to those of *Cassini*'s close flyby of Rhea in Table 1. Voyager II encountered Saturn in August 1981, but passed too far from Rhea (646,000 km versus 74,000 km during Voyager I) to provide a significant improvement of the gravity field determination of this satellite.

[9] The information on the physical state of Rhea inferred from *Cassini* encounter is presented in Table 2. Rhea is a middle-sized icy satellite, with a radius of 764.4 ± 1.1 km [*Thomas et al.*, 2006] determined from Voyager imaging. Its GM is estimated to be 154.0499 ± 0.1060 km^3/s^2 (*Jacobson et al.*, 2005). Combining these data yields Rhea's mean density as $\bar{\rho}$ = 1233 ± 5 kg/m^3.

[10] In this study we use 1233 kg/m^3 and 764 km, as the average density and radius, respectively.

[11] Photometric studies have measured Rhea's average geometric albedo to be about 0.7. The leading hemisphere is actually 20% brighter, with large H_2O ice bands, than the trailing hemisphere [*Buratti et al.*, 1990; *Verbiscer and Verveka*, 1989]. We refer to *Thomas'* [1988] review of the different geologic units identified in Voyager images.

[12] 1. "Cratered terrain I" shows a high density of large diameter craters. This is the oldest terrain with an age of about 3.9 Gyrs.

[13] 2. "Cratered terrain II" does not exhibit craters larger than 40 km in diameter. It covers the previous unit to the east. Its age is estimated between 3.5 and 3.8 Gyrs.

[14] 3. "Equatorial smooth plains material", extending to latitudes of 30 degrees, indicates that the satellite has undergone partial resurfacing at a later stage.Rhea does not show any sign of geodynamical (i.e., internal) activity subsequent to the latter episode. However, we have poor imaging of the trailing hemisphere (≥50 km per line), and we expect the Cassini optical remote-sensing instruments to provide us with more information about the geological history of this satellite.

2.2. Modeling of the Geodynamical and Thermal Evolution

[15] Thermal evolution models of icy satellites are governed by accretional heat, radiogenic decay, tidal heating and latent heat of the mineralogical transitions. They are controlled by ice rheology and location of the layer boundaries.

2.2.1. Thermal Evolution

[16] Models of thermal evolution of Rhea published so far consider radiogenic heating as the main source of energy. Radiogenic heating is a function of the silicate content. It is often considered that medium-sized satellites, such as Rhea, are undifferentiated, since there has not been enough accretional and radiogenic energy to allow for the melting of the ice-rock mixture [e.g., *Ellsworth and Schubert*, 1983; *Schubert et al.*, 1986; *Federico and Lanciano*, 1983; *McKinnon*, 1998]. Computation of the temperature profile after accretion [*Ellsworth and Schubert*, 1983] indicates that temperature might have been high enough for partial differentiation of the 10 to 100 km outermost of Rhea, if all the accretional energy is used to heat the body.

[17] Thermal evolution models feature strong convective transfer [e.g., *Schubert et al.*, 1986; *McKinnon*, 1998], which is responsible for rapid cooling of the satellite. Subsolidus convection rapidly transfers the heat generated by radiogenic decay to the surface, which in turn prevents ice from melting and the separation of the ice from the rock phase.

2.2.2. High-Pressure Polymorph Ice II

[18] For temperature ranges present in medium-sized icy satellites [e.g., *Ellsworth and Schubert*, 1983], high-pressure polymorph ice II is expected to crystallize between 70 and 100 MPa. This pressure range is attained in Rhea.

[19] However, the presence of an ice II layer in the largest Saturnian satellites (not including Titan) has been questioned by *Ellsworth and Schubert* [1983] and *Schubert et al.* [1986]. In *Ellsworth and Schubert*'s [1983] model of thermal evolution, warming of Rhea's interior by radiogenic heating during its first 500 Myrs induced the change of ice II into ice I. The resulting radius increase could be respon-

Table 2. Observational Constraints for Rhea From Voyager I

Parameter	Measurement	References
Radius, km	764.4 ± 1.1	*Thomas et al.* [2006]
GM, km^3/s^2	154.0499 ± 0.1060	*Jacobson et al.* [2005]
Density, kg/m^3	1233 ± 5	*Thomas et al.* [2006]
Angular velocity, rad/s	1.60979×10^{-5}	after *Yoder* [1995]
Semimajor axis, km	527.03×10^3	after *Yoder* [1995]
Tidal parameter q_t	$7.516 \times 10^{-4} \pm 0.064 \times 10^{-4}$	after *Yoder* [1995]

Table 3. Materials and Densities Used in the Models

Material	Density, kg/m^3 Symbol	Range
Rock	ρ_{rock}	2700–3600
Ice I	ρ_I	931–945
Ice II	ρ_{II}	1200
Undifferentiated layer Ice I–silicate	ρ_{Im}	931–3600
Undifferentiated layer Ice II–silicate	ρ_{IIm}	1200–3600

sible for the numerous expression of tensional stresses observed on the surface of the satellite. Subsequent cooling induced the reverse phase change. *Schubert et al.* [1986] argue that the consequent crystallization of ice II would result in a surface area reduction of 4% (i.e., 302×10^3 km^2) while there seems to be no signature of such a reduction in Voyager photogeological observations. However, *Thomas* [1988] identifies compressive features as megaridges and megascarps that folded both the Cratered terrains I and II. The calculation by this author of the surface shortening associated with these features is 25 times smaller than the theoretical calculation by *Schubert et al.* [1986], but it must be pointed out that 60% of Rhea's surface was poorly imaged at the time these studies were published.

[20] Models by *Anderson et al.* [2003] do not include an ice II layer. In the present study we consider the presence of such a layer, based on the following arguments. First, tectonic processes shaping the surface of icy satellites are not fully understood. Moreover, considering the average resolution of Voyager imaging of Rhea, it is premature to rule out the existence of ice II only on the basis of photogeological arguments.

[21] This issue is of primary importance as it is a clue to understanding the conditions of the environment in which Rhea formed and evolved. As explained by *Ellsworth and Schubert* [1983], absence of ice II would imply a "hot" temperature profile (internal highest temperature of 160 K instead of 130 K), inappropriate for ammonia hydrates to condense. This would require supplemental sources of energy not considered in usual models of internal dynamics of Rhea, such as tidal heating. Upcoming high-resolution imaging of Rhea by Cassini will provide better material with which to reconsider this issue.

2.2.3. Role of NH_3

[22] *Consolmagno and Lewis* [1978] and *Stevenson* [1982] consider that partial melting may have occurred during the thermal evolution of the body, owing to the presence of ammonia and salts of chondritic origin mixed with water. The consequent decrease of the eutectic temperature could have led to partial or even entire differentiation. *Consolmagno* [1985] concluded that the only scenario of evolution accounting for the morphological features observed at the surface of Rhea is the ammonia-water refreezing model. Furthermore, he stressed that such a model can explain the differences observed in the morphology of the different Saturnian satellites. The validity of such a scenario has been questioned by *Schubert et al.* [1986] and more recently by *Hogenboom et al.* [1997] on the basis of new experimental measurements of the properties of ammonia-water mixtures.

[23] Models of thermal evolution in absence of NH_3 or salts have been calculated by *Ellsworth and Schubert* [1983] as a function of initial energy. The results indicate that solid-state convection in Rhea might have lasted 3.3 Gyr, independently of the initial temperature. The resulting temperature profile lies below 130K for present Rhea. In absence of any other reference, we use this temperature profile for the models considered in the present study.

2.2.4. Comment on Geodynamical Models

[24] It is important to note that the thermal evolution models mentioned above are isoviscous and consider only radiogenic heating as the main source of energy. Some models point out the short-lived isotope Al^{26} as a potentially crucial source of energy during the early evolutionary stages of icy bodies, that could have been responsible for their partial to extensive melting [*Prialnik and Bar-Nun*, 1990]. A recent study by *Castillo et al.* [2005] indicates that ^{26}Al could have played a crucial role in Iapetus' thermal and dynamical evolution. This requires that the formation of satellites in Saturn's subnebula was rapid enough with respect to the lifetime of short-lived radiogenic species. We have poor constraints with regards to this matter in the case of Rhea. However, since Rhea's rock mass fraction is 50% greater than the one of Iapetus, the effect of ^{26}Al could have created a significant increase in internal temperature in the early history of the satellite, likely to trigger its partial to full differentiation [*Prialnik and Bar-Nun*, 1990]. Tidal heating is not considered as a significant source of energy in Saturn's satellite evolution models, except for Enceladus.

[25] Recent models of thermal transfer in medium-sized satellites [*Rainey and Stevenson*, 2003] include temperature dependent viscosity, and temperature and pressure dependent conductivity. A remarkable result of this study is the possibility of maintaining a deep ocean inside icy satellites of radius less than 1000 km. These author show that it is possible to differentiate Rhea and to preserve an ocean inside this body provided that small amounts of volatiles such as ammonia dihydrates are present.

[26] We do not include a deep ocean in the models of the present study considering that (1) we have poor constraints on the characteristics of such a deep ocean inside Rhea and (2) the difference in density between water ice and liquid water is too small to have a significant signature on the moment of inertia. A liquid layer inside Rhea could theoretically be detected by determination of the dynamic potential Love number k_2. However, its signature would not represent more than 0.2% of C_{22}.

[27] None of the works referred to in this section consider the differentiation of an iron core as a plausible outcome of the satellite's evolution. These models do not produce enough heat for the separation of iron from the silicate. Hence the models considered in this paper do not include an iron core.

2.3. Material Properties

[28] The densities of the different materials involved in the models are presented in Table 3.

2.3.1. Porosity

[29] The maximum pressure reached in Rhea's interior is ~125 MPa. Due to self-compression and internal warming, porosity decreases rapidly inside Rhea's interior [e.g., *Leliwa-Kopystynski and Kossacki*, 2000]. A few kilometers below the surface porosity becomes negligible. Thus we assume that it plays a little role on changing the bulk density

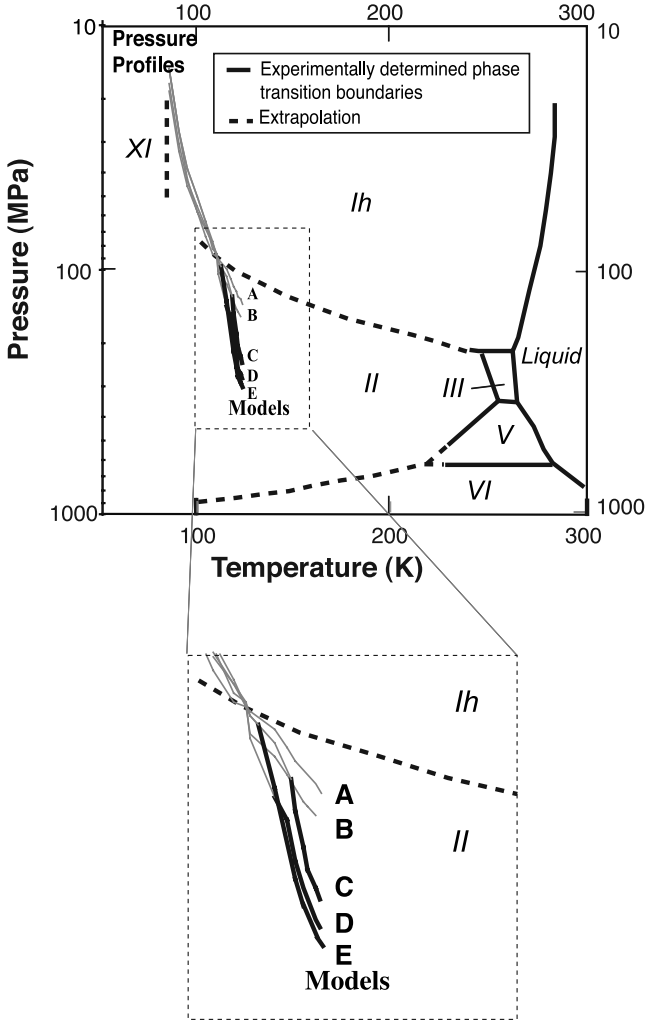

Figure 1. Water phase diagram, after *Petrenko and Whitworth* [1999]. Pressure/temperature profiles are featured for examples of the different types of models in which the silicate density is set to 3300 kg/m^3. Thick segments correspond to the silicate core in models of types C, D, and E.

of Rhea and we consider that Rhea's density is characteristic of the bulk density.

2.3.2. Rock Phase

[30] We refer to the "rock phase" as the association of the silicate component and the metallic phase (Fe-FeS, Ni). The icy satellite literature has a number of different compositions for the rock phase. The rock density is a function of the composition of the accreted chondrites together with possible alteration of the silicates due to metamorphic reactions during the evolution of the satellites. *Lupo and Lewis* [1979] consider dehydrated silicate with the ordinary chondritic composition, corresponding to a density of 3650 kg/m^3. Carbonaceous chondrites are another possible starting material [*Kargel*, 1998; *Scott et al.*, 2002], with hydrous silicate densities lower than 3000 kg/m^3. *Scott et al.* [2002] and *Zolotov et al.* [2002] speculate that during accretion and evolution, fluid circulation in satellites saw conditions of moderate pressure and moderate to high temperature (<1000K) and the metamorphic alteration of olivine and pyroxene into serpentine and other hydrated minerals. *Schubert et al.*'s [1986] temperature profile in Rhea, indicates that at least in the early evolution of this satellite, conditions were suitable for hydrothermal phenomena to occur. After *Scott et al.* [2002] the minimum density for the hydrous silicate component of the icy satellites is 2700 kg/m^3 and this will be our lower limit.

[31] Some studies [e.g., *Lupo*, 1982; *Anderson et al.*, 2003] consider that the density of the Saturnian satellite rock component must match the density of Io, i.e., 3527.8 ± 2.9 kg/m^3 [*Anderson et al.*, 2001]. This is based on the model that Io represents the icy-satellite refractory component. Such an assumption requires some caution. Io's density is representative of the non-ice phase of the large satellites of Jupiter, but might happen to be a poor reference for the medium-sized satellites of Saturn, because the evolution of their environments may have been significantly different [*Kargel*, 1998]. Also, the average temperature reached within Io during its evolution is thought to be much higher than the temperature range seen in the small Saturnian satellites. There is little doubt that Io's rock component is dehydrated owing to radiogenic and tidal heating [e.g., *Zolotov et al.*, 2002]. We lack similar strong constraints in the case of Saturn's satellites.

[32] In this study, we consider variations of the rock density from 2700 to 3600 kg/m^3. This allows us to model the different assumptions described above. For the ranges of pressure and temperature in Rhea, the variations in the rock phase density are negligible.

2.3.3. Icy Layer

[33] A temperature of about 110K is expected for Rhea at a depth of around 400–450 km [*Ellsworth and Schubert*, 1983]. There, at this temperature, ice I transforms into its polymorph ice II, at a pressure of ~90 MPa (Figure 1). Nevertheless we must bear in mind that the Clapeyron slopes in this range of pressure and temperature have not been very well determined. Besides, as discussed by *Lupo and Lewis* [1979], this phase could also be metastable even at geological timescales in these conditions of pressure and temperature, especially if ammonia is present.

[34] Experimental measurements of ice I density yield a density of 931 kg/m^3 for Rhea's surface conditions [e.g., *Bridgman*, 1937]. Ice II properties are poorly documented. Ab-initio measurements by *Fortes et al.* [2003] yield an ice II zero pressure and temperature density of 1240.27 ± 0.62 kg/m^3. Previous laboratory measurements by *Gagnon et al.* [1990] had yielded a density of 1193 kg/m^3, at a pressure of 283 MPa and a temperature of 237.5 K. *Lupo and Lewis* [1979] also present the following equation of state, based on a compilation of laboratory measurements of the behavior of ice II as a function of pressure and temperature:

$$\rho_{II(g/cm^3)} = 1.1711 + P_{(MPa)} \times 8.96 \times 10^{-6} - T_{(K)}\left(7.9 \times 10^{-5}\right) \quad (1)$$

This equation yields a density of 1177 kg/m^3 in the conditions applied by *Gagnon et al.* [1990], and thus differs by less than 1.5% with the value of density measured by the latter authors. On the other hand, the zero pressure and temperature density inferred from equation (1), equal to

1171 kg/m^3, is largely inconsistent with *Fortes et al.* [2003]. This means that we have no reliable value of ice II density for the conditions expected in Rhea's interior, roughly a pressure 85–100 MPa and a temperature around 100 K (see *Schubert et al.* [1986] and Figure 1). We choose to use a density equal to 1200 kg/m^3.

2.3.4. Undifferentiated Layer

[35] As suggested in the thermal evolution models (previously discussed in section 2.2), we consider the possibility that the body might be only partially differentiated. We include in the models homogeneous layers of ice mixed with the rock phase. We refer to x as the mass fraction of rock. As a function of x, and of the density of the rock phase, the density of these layers varies from 931 kg/m^3 to 3600 kg/m^3.

[36] The rock density and the rock mass fraction are two unknowns that blur the discrimination among composition models. For example, a layer with a density of 3000 kg/m^3 can be composed either of hydrated silicate or of a mixture of ice and dehydrated silicate.

2.4. Modeling Rhea

[37] Now we present the Rhea interior models and discuss their characteristics. The approach considered in this study assumes hydrostatic equilibrium. As discussed in section 4.2.2, nonhydrostatic anomalies, due for example to heterogeneities at the rocky core–ice shell interface, are likely to affect the gravity signal and thwart the proper interpretation of this data into interior models.

2.4.1. Profiles

[38] The boundaries between the different layers are determined by combining the pressure and temperature profiles, together with satellite's mean radius and density.

2.4.1.1. Pressure Profile

[39] Hydrostatic pressure, P, is calculated as a function of the radius, r, by integration of the following equation:

$$\frac{dP}{dr} = -\rho(r)g(r), \tag{2}$$

where $\rho(r)$ is the density profile.

[40] The gravity profile, $g(r)$, is computed from

$$g(r) = \frac{4\pi}{3} G \int_0^r \rho(r) r^2 dr, \tag{3}$$

where G is the universal gravitational constant.

2.4.1.2. Temperature Profile

[41] The most recent work on the temperature profile is by *Schubert et al.* [1986]. We use their models of temperature distribution as a function of depth. Pressure-temperature profiles for representative examples of each model category are presented in Figure 1.

2.4.1.3. Self-Compression Effects

[42] Density variations as a function of pressure are accounted for following the equations presented by *Lupo and Lewis* [1979] for ice I,

$$\rho_{I(g/cm^3)} = 0.9403 + \left(1.143 \times 10^{-4}\right)\left(P_{(MPa)} \times 10 - 1\right)^{0.737} - T_{(K)}\left(8.585 \times 10^{-5}\right). \tag{4}$$

For the range of pressure and temperature present in Rhea's interior, ice I density varies from 931 kg/m^3 at the surface to 945 kg/m^3 at the transition with ice II. In the case of ice II, we lack the information necessary to compute this effect (see section 2.3). The effect of self-compression on the rock component for the pressures encountered in medium-sized satellites is negligible (lower than 0.05%).

2.4.1.4. Ice I ↔ Ice II Phase Transition

[43] The depth of the ice I ↔ ice II transition, hereafter called $r_{I\text{-}II}$, is inferred from the combination of the temperature and pressure profiles, and *Petrenko and Whitworth*'s [1999] water phase diagram (see Figure 1 and section 2.4.3).

2.4.1.5. Density of the Undifferentiated Layers

[44] We consider that the undifferentiated layers are radially of the same composition and laterally homogeneous. The effect of ice density variations with depth is negligible with respect to the density of silicate. As the silicate density does not vary with depth, we consider that the densities of undifferentiated layers are constant. The density of a layer made of ice of density ρ_{ice} and rock of density ρ_{rock} with a mass fraction x is defined as

$$\frac{1}{\rho_m} = \frac{x}{\rho_{rock}} + \frac{1-x}{\rho_{ice}}, \tag{5}$$

where x is the rock mass fraction. We hereafter refer to ρ_{Im} and ρ_{IIm} as the densities of undifferentiated layers composed of rock and ice I or of ice II, respectively.

2.4.2. Density Profile Calculation

[45] For each model type, we vary the rock phase density, and, depending on the model type, the rock-ice I mixture density within the ranges defined in Table 3. We also vary r_2, the bottom radius of the outer icy layer, in models of type II and IV. The rock-ice II mixture density is inferred from ρ_{1m}, after equation (5).

[46] We apply the following algorithm, in order to determine (1) the density profile in the ice and ice-mixture layers, (2) the location of the ice I ↔ ice II transition radius, and (3) the rocky core radius. The body, assumed spherical, is divided in 1-km-thick sublayers. Densities are initialized constant in each sublayer of a given layer, i.e., ρ_{rock} in the rocky core, $\rho_{ice}^{init} = 931$ kg/m^3 in the ice shell, etc. Pressure is computed for this configuration using equations (2) and (3). The ice I ↔ ice II boundary is inferred from the water phase diagram (Figure 1 and corresponding equations of state from *Petrenko and Whitworth* [1999]). Densities in the ice and ice and rock mixture shells are recalculated as a function of pressure and temperature (equation (4)). The consequent overall mass change is accommodated in the core radius. The pressure profile is then corrected on the basis of the updated density profile. The different steps of this calculation are iterated until the difference between the pressure profiles at the iteration i and $i + 1$ becomes lower than 0.5%.

2.4.3. Categories of Models

[47] Combining the pieces of information presented in sections 2.1, 2.2, and 2.3, five main categories of models can be devised (Figure 2). These differ by their degree of differentiation. Inside each of these categories, we define two subtypes depending on the presence or absence of an ice II layer. Observational constraints on the models are the

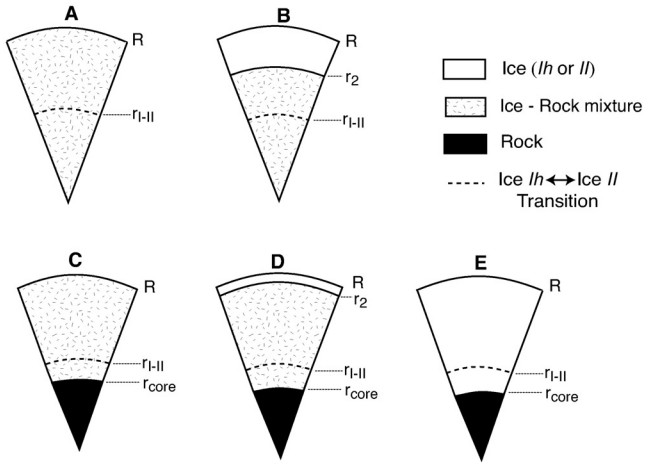

Figure 2. Categories of models for Rhea.

bulk density and the mean radius. We present below the equations linking the parameters involved in the modeling. For convenience of presentation, we use ρ_I as an average for the ice I layer (temperature- and pressure-dependent) density inferred from the numerical calculation described in the previous paragraph. The parameters to solve for are listed in Table 3. The main characteristics of the models as inferred from the calculation are presented in Table 4.

2.4.3.1. Undifferentiated Models (Type I)

[48] For models with no ice II, density variations are governed by the effect of self-compression.

Models with ice II

$$R^3\overline{\rho} = r_{I-II}^3\rho_{IIm} + \rho_{Im}\left(R^3 - r_{I-II}^3\right). \tag{6}$$

The ice-rock mixture density ρ_{Im} varies from 1190 to 1195 kg/m^3 as a function of the rock phase density, implying variation of ρ_{IIm} from 1466 to 1486 kg/m^3. Ice I ↔ ice II transition takes place at about 410 km depth.

2.4.3.2. Two-Layered Models (Types B, C, and E)

[49] Models of type B consist of a core made of a mixture of ice and rock overlaid by an icy layer. The interface between the ice shell and the core is located at radius r_2 such that

Models with ice II

$$R^3\overline{\rho} = r_{II}^3\rho_{IIm} + \rho_{Im}\left(r_2^3 - r_{I-II}^3\right) + \rho_I\left(R^3 - r_2^3\right) \tag{7}$$

Models with no ice II

$$R^3\overline{\rho} = \rho_{Im}r_2^3 + \rho_I\left(R^3 - r_2^3\right). \tag{8}$$

For different values of the variable r_2 we infer the core density and determine the location of the ice I ↔ ice II transition, which varies between 408 and 450 km.

[50] Models of type C: are made of a rocky core and an undifferentiated ice-rock mantle. Variables are the rock phase density and the mass fraction of the ice-rock mixed layer. The rocky core radius r_{core} is inferred from the following equations:

Models with ice II

$$r_{core} = \left[\frac{R^3(\overline{\rho} - \rho_{Im}) - r_{I-II}^3(\rho_{IIm} - \rho_{Im})}{\rho_{rock} - \rho_{IIm}}\right]^{\frac{1}{3}}. \tag{9}$$

The ice I ↔ ice II transition radius varies between 409 to 415 km, as a function of the rock phase density.

Models with no ice II

$$r_{core} = \left[\frac{R^3(\overline{\rho} - \rho_{Im})}{\rho_{rock} - \rho_{Im}}\right]^{\frac{1}{3}}. \tag{10}$$

[51] Models of type E have a rocky core fully differentiated from an ice mantle. These are the models considered by *Anderson et al.* [2003]. Calculations indicate that the pressure of transformation of ice I into ice II is reached for most values of the core radius, a feature that was not taken into account by *Anderson et al.* [2003]. The rocky core radius r_{core} is thus inferred from the following equations:

Models with ice II

$$r_{core} = \left[\frac{R^3(\overline{\rho} - \rho_I) - r_{I-II}^3(\rho_{II} - \rho_I)}{\rho_{rock} - \rho_{II}}\right]^{\frac{1}{3}}. \tag{11}$$

The ice I ↔ ice II transition takes place at about 408 km.

Models with no ice II

$$r_{core} = \left[\frac{R^3(\overline{\rho} - \rho_I)}{\rho_{rock} - \rho_I}\right]^{\frac{1}{3}}. \tag{12}$$

2.4.3.3. Three-Layered Models (Type IV)

[52] Models of type D are the most complex but also the more realistic representations of satellites such as Rhea. Variable parameters are the bottom radius of an outer icy layer, the rock density and mass fraction in undifferentiated layers, and the core radius. These parameters are linked through the following equations:

Models with ice II

$$R^3\overline{\rho} = r_{core}^3\rho_{rock} + \rho_{IIm}\left(r_{I-II}^3 - r_{rock}^3\right) + \rho_{Im}\left(r_2^3 - r_{I-II}^3\right) + \rho_I\left(R^3 - r_2^3\right). \tag{13}$$

Table 4. Main Structural Characteristics of the Different Models Presented in Figure 2[a]

Models	Variables	r_2, km	Rocky Core Radius r_{core}, km	$r_{I\text{-}II}$, km
Models A	ρ_{rock}, x	...	...	~410
Models B	r_2, ρ_{rock}, x	465–764	...	408–450
Models C	ρ_{rock}, x, r_{core}	...	0–411	409–415
Models D	r_2, ρ_{rock}, x	350–764	346–41	408–450
Models E	ρ_{rock}, r_{core}	...	346–411	~409

[a]For each model are indicated the variables to solve for and the bounds on r_2, r_{core}, and $r_{I\text{-}II}$ inferred from the calculation. The parameter x corresponds to the rock phase mass fraction.

Table 5. Ranges for the Values of Silicate Mass Fraction, C_{22} and the Differences Between the Polar and the Equatorial Radii ($a-c$) for the Models Presented in Figure 2

Model	Silicate Mass Fraction Range	C_{22}	$a-c$, km
A	0.29–0.34	$2.63–2.80 \times 10^{-4}$	2.76–2.86
B	0.28–0.36	$1.78–2.80 \times 10^{-4}$	2.28–2.86
C	0.29–0.37	$1.93–2.80 \times 10^{-4}$	2.32–2.86
D	0.27–0.37	$1.68–2.80 \times 10^{-4}$	2.16–2.86
E	0.31–0.37	$1.68–1.77 \times 10^{-4}$	2.16–2.22

The outer icy layer bottom radius r_2 is ranged between the mean radius and the ice I $\Longleftrightarrow$ II boundary. Then the core radius r_{core} is inferred from equation (13).

Models with no ice II

$$R^3\overline{\rho} = r_{core}^3\rho_{rock} + \rho_{Im}\left(r_2^3 - r_{rock}^3\right) + \rho_I\left(R^3 - r_2^3\right). \quad (14)$$

For each value of the outer icy layer bottom radius r_2, r_{core} is inferred from equation (14), under the constraint that $r_2 < r_{core}$. When the core radius tends toward zero, models of type D become similar to models of type B. When the mantle density tends toward the density of ice I, models of type C are similar to models of type E.

[53] Rock mass fractions for the different models of this study range from 0.27 to 0.37 as a function of the rock phase density and of the degree of differentiation (Table 5), in agreement with *Schubert et al.* [1986].

3. Links Between Gravity Field and Interior Models

3.1. Gravity Field Equations

[54] We recall the equations that link the properties of a planetary body interior to its gravity field, i.e., the observable. Following the demonstration proposed by *Anderson et al.* [2003], we assume that Rhea is in hydrostatic equilibrium. This assumption will be discussed in further details in section 4.2.

[55] To second order, the gravitational potential of a rotationally and tidally distorted synchronously rotating satellite in a spherical orbit is [*Kaula*, 1966],

$$V(r,\phi,\lambda) = \frac{GM}{r}\left[1 + \left(\frac{R}{r}\right)^2\left[C_{20}\left(\frac{3}{2}\sin^2\lambda - \frac{1}{2}\right) + 3C_{22}\left(\cos^2\lambda\cos 2\phi\right)\right]\right], \quad (15)$$

where r, λ, and ϕ are the radius, latitude, and longitude, respectively, C_{20} and C_{22} are the degree two gravity coefficients. The parameter J_2 is defined such that $J_2 = -C_{20}$. C_{22} and J_2 are linked to the internal structure through the moment of inertia I,

$$I = \frac{8\pi}{3}\int_c^R \rho(r)r^4 dr. \quad (16)$$

[56] We consider the mean moment of inertia, assuming the body to be spherical. This approximation is reasonable if one consider that for a hydrostatic figure, the different between Rhea's equatorial and polar radii is of the order of 2.5 km (see section 4.3).

[57] We introduce the secular (or fluid) Love number k_s, which is linked to the dimensionless moment of inertia through the Radau-Darwin Approximation,

$$k_s = \frac{4 - Q^2}{1 + Q^2}, \quad (17)$$

where

$$Q = \frac{5}{2}\left(1 - \frac{3}{2}\frac{C}{MR^2}\right), \quad (18)$$

where C is the polar moment of inertia. As justified before, approximating Rhea as a sphere allows to set that $C \sim I$.

[58] The degree-two gravity coefficients are derived from

$$C_{22} = \frac{1}{4}k_s q_t, \quad (19)$$

with q_t being the tidal parameter. The latter parameter is computed from the following equation:

$$q_t = \frac{M_p}{M}\left(\frac{R}{D}\right)^3, \quad (20)$$

where M is the satellite's mass, M_p Saturn's mass and D, Rhea's semimajor axis. Uncertainties in the most recent values of the parameters involved in the definition of q_t, result in an uncertainty of 6×10^{-6} (i.e., <1%) on this parameter.

[59] We compute successively the equations (16), (17), (18) and (19)–(20) for each interior model. Variations of C_{22} as a function of the core radius are plotted in Figures 3 to 5.

3.2. Variations of C_{22}

[60] The values of C_{22} for the whole set of models ranges from 1.68×10^{-4} to 2.80×10^{-4}. Details for each category of model are presented in Table 5. The distribution of the different models in the $r_{core} - C_{22}$ space is presented in Figure 3. This plot shows that (1) models of type B, C, and E are end-members of models of type D; (2) models of type A are end-members of models of types B and C; and (3) Models of type E are also end-members of models of type C. The difference in the value of C_{22} as a function of the presence of ice B decreases as the degree of differentiation of the models increases (Figures 4 and 5).

3.2.1. Undifferentiated Models (Type I)

[61] In models with no high-pressure ice, C_{22} varies between 2.63 and 2.65×10^{-4} as a function of the rock phase density. The corresponding values of C/MR^2 vary between 0.388 and 0.389. These are lower than the value of 0.4 for a homogeneous body, owing to the fact that the presence of high-pressure ice II results in shifting the density concentration toward the center of the satellite. Undifferentiated models with no ice II are characterized by a value of C_{22} equal to 2.8×10^{-4}. This differs by 6% from the corresponding value for models with high-pressure ice.

3.2.2. Differentiated Models (Type V)

[62] The smallest values of C_{22} are reached for models of type E, i.e., differentiated into a rocky core and an ice

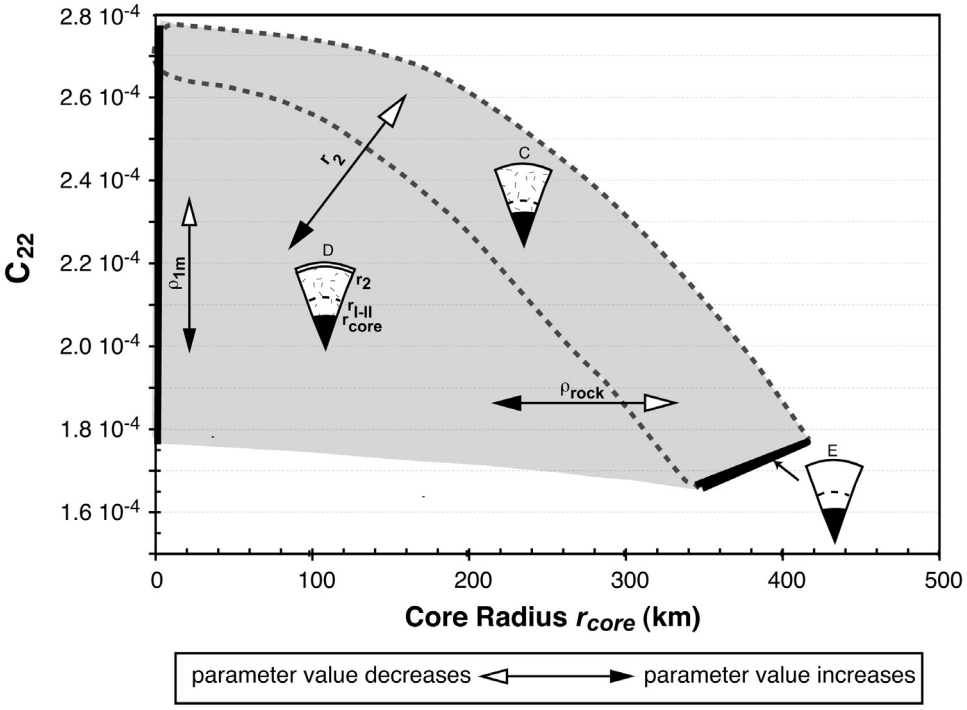

Figure 3. Variations of C_{22} as a function of the rocky core radius for different types of Rhea models, and Table 3 input parameter ranges. Arrows indicate the relative variations of the rock density, the bottom radius of the outer icy shell, and the ice-rock mixture density. Models A and B lie on the *y* axis. Models of type A correspond to $C_{22} > 2.65 \times 10^{-4}$. The dashed line bounds the space corresponding to models of type C. It overlaps the region (dark gray) corresponding to models of type D.

mantle (Figure 4). As a function of the rocky core radius, C_{22} varies between 1.67×10^{-4} and 1.77×10^{-4}. The difference in C_{22} between models with ice II and the ones without ice II is less than 0.2%. For a given value of C_{22}, there is an uncertainty of only 10 km on the derived core radius, due to the effect of ice II.

3.2.3. Partially Differentiated Models (Types B, C, and D)

[63] In these cases, we note that for the different models the ranges of C_{22} overlap (Figure 3 and Table 5). This is due to the numerous parameters involved in the models, some of which are poorly constrained (such as the rocky phase density and mass fraction).

[64] We note also that C_{22} is less sensitive to the rock phase density for models that include a layer composed of a mixture of ice and rocks. As the density of the rock phase increases, the slope of C_{22} tends toward zero and changes sign. When C_{22} becomes greater than 2.00×10^{-4} changing the rock phase density from 2700 to 3600 kg/m^3 results in a change in C_{22} of less than 3%. Owing to the weak dependence of C_{22} on rock density for models of types B, C and D, uncertainty in the rock phase density results in an uncertainty on the core radius of up to 300 km. The maximum radius of a rocky core, if present, decreases when the value of C_{22} increases. It becomes lower than 100 km for C_{22} greater than 2.7×10^{-4} (Figures 3 and 5).

[65] The model dependence of C_{22} as a function of the core radius and the bottom radius of the outer icy shell is represented in Figure 5. For that case the rocky core density has been set to 3300 kg/m^3, close to the density for an average chondritic composition. C_{22} provides an upper bound on the icy outer shell thickness. For example, a value of C_{22} equal to 2.42×10^{-4} corresponds to a value of r_2 equal to the difference between 700 ± 30 km and 764 km, i.e., an outer icy shell thinner than 64 ± 30 km. The uncertainty on the latter determination is due to the effect of ice II. This uncertainty decreases with decreasing values of C_{22}.

4. Improvement in Model Parameters

[66] The purpose of this section is to look forward and to identify the information that will be acquired on Rhea's interior in the foreseeable future from gravity field measurements such as those described by *Anderson et al.* [2003], and the uncertainties that will be associated with the data. We consider also the synergy between radio science measurements and the observations provided by other Cassini instruments that can provide us with some of the information we lack.

4.1. Covariance Analysis Results

[67] The covariance analysis simulation by *Anderson et al.* [2003] indicates that Rhea's C_{22} will be determined to an absolute accuracy ΔC_{22} of $\pm 1 \times 10^{-6}$ to $\pm 7 \times 10^{-6}$. This corresponds to a relative accuracy of about 0.5 to 3.5%, respectively. These error bars are represented for different values of C_{22} in Figures 4 and 5.

[68] A value of C_{22} between 2.63×10^{-4} and 2.80×10^{-4} indicates that the body is undifferentiated. Further conclusions can be drawn about the thermal evolution of

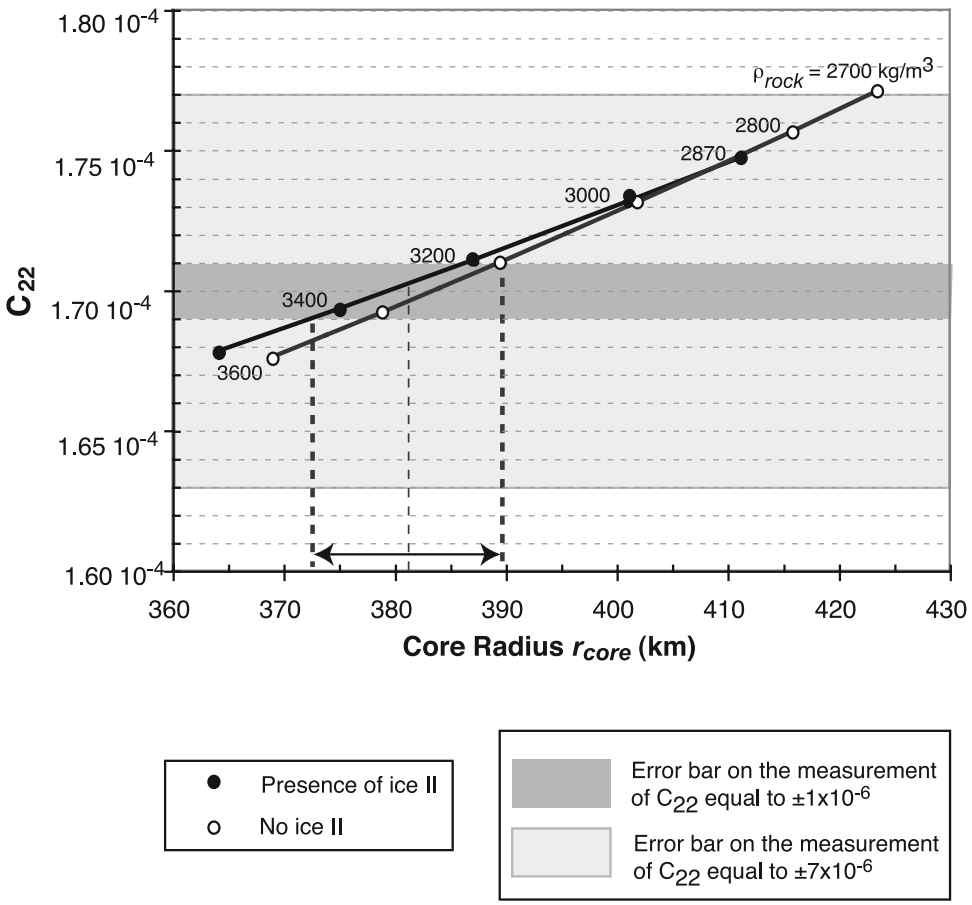

Figure 4. Variations of C_{22} as a function of the rocky core radius (r_{core}) and density (ρ_{rock} in kg/m^3) for models of types E. The error bars expected on the measurement of C_{22} [*Anderson et al.*, 2003] by Cassini are plotted for a value of C_{22} equal to 1.70×10^{-4} taken as an example. Vertical lines indicate the corresponding uncertainties on the determination of the core radius.

Rhea. This suggests that there has not been enough energy available during the history of this satellite to allow for full melting of ice and the consequent segregation of the rock phase, and to balance heat transfer through subsolidus convection. This also provides some constraint on the presence and the role of ammonia dihydrate and other contaminants likely to decrease the water eutectic temperature.

[69] If C_{22} is higher than 2.65×10^{-4} and close to 2.80×10^{-4} (i.e., C/MR^2 close to 0.4), conditions are not suitable for ice II to be stable, and thus the body is radially homogeneous except for slight concentration of mass toward the center due to self-compression.

[70] If C_{22} is lower than 1.80×10^{-4}, the rock is fully differentiated from the ice. The core radius can be determined using equation 11 or 12, depending on the assumption on the presence of ice II. The uncertainty in the measurement of C_{22} of $\pm 1 \times 10^{-6}$ yields r_{core} up to ±8 km (Figure 4). If ΔC_{22} is $\pm 7 \times 10^{-6}$ the error on the core radius determination becomes ±30 km. Then it is not possible to get an accurate information on the core radius, and thus the composition (especially hydration state) of the silicate.

[71] In the interval between the extreme values (1.80×10^{-4} and 2.60×10^{-4}), we have a large uncertainty in the characteristics of Rhea's internal structure, unless we choose an a priori model for the satellite. Further assumptions on the rock phase density and the presence or absence of ice II might be necessary to narrow the field of possible models.

[72] For a given model, the influence of the rock phase density on C_{22} decreases when the latter parameter increases, and is ineffective when C_{22} becomes greater than 2×10^{-4}. Furthermore, we expect that other measurements performed by Cassini will provide constraints on the nature of the silicate component of the Saturnian satellites, although it is possible that the silicate has evolved from its original state, for example through hydrothermal metamorphism.

[73] It is important to note that the 6% difference in C_{22} between undifferentiated models with and without a high-pressure layer of ice II is higher than the expected uncertainty on C_{22}. The influence of ice II on C_{22} decreases when the latter parameter tends toward low values. Supplementary information, for example inferred from photogeology, might help constrain the presence of high-pressure ice in the body. Then if we consider for example the case of models of type B and D, the uncertainty in the measurement of C_{22} translates into an uncertainty in the estimation of the minimum outer ice shell thickness of 5 to 40 km, comparable to the uncertainty due to the effect of ice II (Figure 5).

[74] If the value of C_{22} happens to be smaller than 1.67×10^{-4}, this is an indication either that the rock phase density is higher than the maximum value considered in this study,

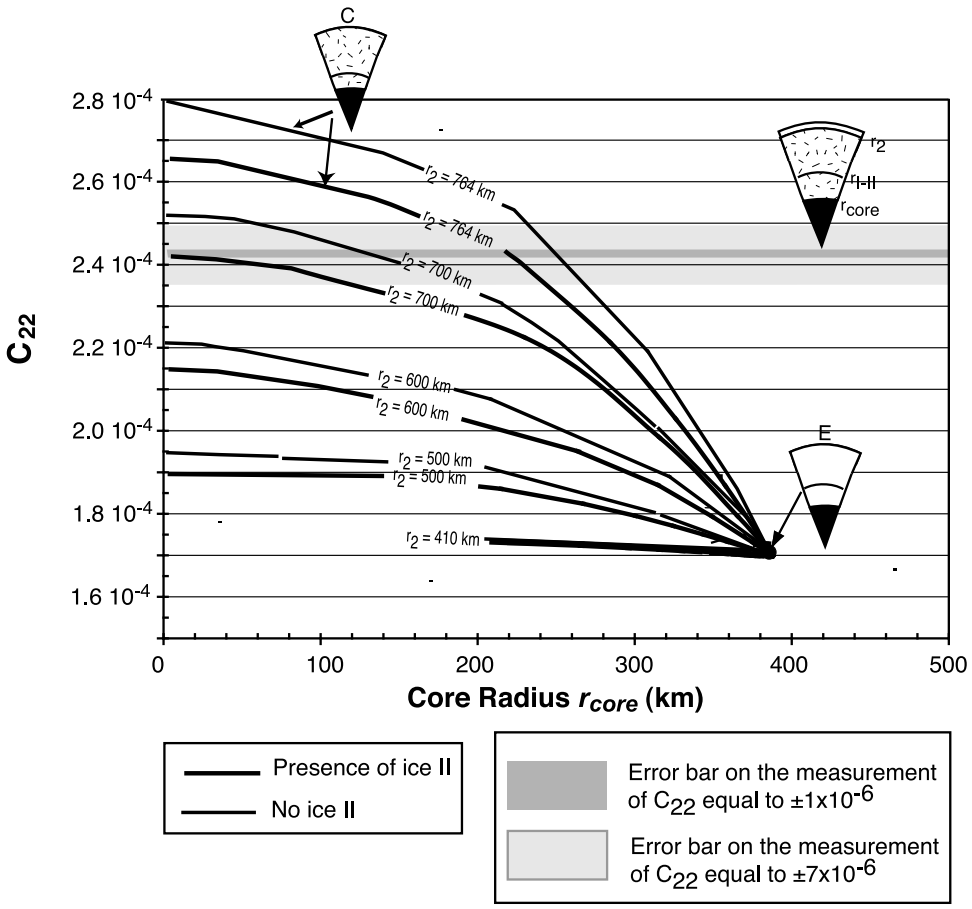

Figure 5. Variations of C_{22} as a function of the rocky core radius and the bottom radius r_2 of the outer icy shell for models a rock phase density set to 3300 kg/m^3. The error bars expected on the measurement of C_{22} by Cassini are plotted for a value of C_{22} equal to 2.42 $\times$ 10^{-4} discussed in the text.

or that there is separation of iron from the silicate phase to form an iron core. As justified in section 2, we have not devoted any special attention to this case, as models of thermal evolution agree that there has not been enough energy released during the evolution of the body to allow for further differentiation. Detecting the presence of an iron core would be a crucial constraint and input to models of thermal evolution.

4.2. Modeling Assumptions

[75] This section discusses the validity of the assumptions we have made about the model parameters.

4.2.1. Density Profile Errors

[76] The most important source of error in the density profile comes from our limited knowledge of the ice II density for the pressure and temperature conditions in Rhea's interior. Available zero pressure and temperature densities vary from 1171 kg/m^3 (*Bridgman* [1937] laboratory experiments) to 1240 kg/m^3 (*Fortes et al.* [2003] ab initio measurements). The difference between ice II density measurements of *Gagnon et al.* [1990] and *Bridgman*'s [1937] ice II equation of state for a pressure of 283 MPa and a temperature of 237.5K is of the order of 1.2%. A rough calculation, based on equation (1), shows that around 110 K, and for a variation of pressure from 85 to 145 MPa (as expected for example between the bottom and the top of the ice II layer in representatives models of type D) the change of density is lower than 0.5%.

[77] We have also taken as a reference the temperature profile proposed by *Ellsworth and Schubert* [1983]. Temperature profile plays a role in the evolution of the materials' density with depth, and on the location of the ice I–ice II transition. A difference of 10 K changes ice I density by less than 0.1%. At 400 km depth, this temperature change results in a maximum shift of the transition depth upward by 70 km. Maximum consequent changes in the value of C_{22} are about 2.5%. The cumulative error due to the uncertainty in the density profile is of the order of the maximum uncertainty expected for the determination of C_{22} from Cassini measurements.

[78] In general, to leverage the quality of the interpretation of the small icy satellites gravity field data in terms of internal structure we need to refine our knowledge of the properties of the materials involved in the models. This remark especially applies to the case of high-pressure ice polymorphs' physical properties. We also need better understanding of the properties of ice and rock mixtures in order to improve modeling of heat transfer (see *Durham and Stern* [2001] for an exhaustive review of the state of knowledge of ice rheological properties). Numerous laboratory measurements performed in the last decade have enhanced our knowledge of the ammonia-water system,

but the effect of other minor chemical components, such as sulfates, methanol, CO_2 (carbonaceous chondrites) are much less characterized. In summary, it is critical that the level of knowledge of the properties determined in the laboratory become available for optimal interpretation of the observations provided by Galileo, Cassini and in the future by the Jupiter Icy Moon Orbiter.

4.2.2. Hydrostatic Equilibrium

[79] The demonstration presented in this article is based on the assumption that the bodies are in hydrostatic equilibrium. However, different studies [e.g., *Mueller and McKinnon*, 1988; *McKinnon and Desai*, 2003] discuss the fact that nonnegligible nonhydrostatic contributions to J_2 and C_{22} might be expected in icy satellites. These anomalies can be due to topography anomalies supported in homogeneous satellites and/or mascons at the rock-icy boundary in differentiated satellites. *Chzechowski and Leliwa-Kopystynski* [2002] also suggest that convection processes taking place within Rhea could create large-scale topography anomalies and lateral density variations. Their study does not provide further quantitative information on the amplitude of these anomalies.

[80] Recent imaging of Iapetus by Cassini indicates that this body, similar in size and in bulk density as Rhea, shows large-scale deviations from sphericity of up to 10 km in amplitude [*Denk et al.*, 2005]. It is possible that similar topographic anomalies will be detected in Cassini high-resolution images of Rhea. Also, recent analysis of Galileo gravity science measurements at Ganymede by *Anderson et al.* [2004] clearly indicates the presence of mascons, localized at the core-ice shell interface (see *Palguta et al.* [2004] for details about the characteristics of these mascons).

[81] Following *Mueller and McKinnon*'s [1988] approach (their equation (7), also referred to as Kaula's rule), we evaluate the nonhydrostatic contributions that can be supported in homogeneous and differentiated Rhea's models by scaling them to the Moon's degree-two gravity coefficients. In both cases the maximum contribution to the gravity signal of nonhydrostatic anomalies supported by Rhea are about 4×10^{-4}. This is twice larger than Rhea's maximum hydrostatic C_{22}. Hence such anomalies would overwhelm the gravity signal.

[82] *Anderson et al.* [2003] questioned the validity of scaling Rhea's nonhydrostatic contributions with respect to the Moon. It can be argued that if mascons exist in a body as large as Ganymede, it is not unreasonable to expect similar features in smaller bodies, with much less energy involved in geodynamical processes and internal evolution.

[83] Hydrostatic equilibrium can be assessed by comparing the moment of inertia inferred independently from J_2 and C_{22}, if both parameters are available with good accuracy. However, *Anderson et al.* [2003] indicate that owing to the flyby geometry (equatorial), Rhea's degree-two gravity coefficient cannot be obtained independently from each other. Determining the moment of inertia without assuming hydrostatic equilibrium requires the measurement of Rhea's rotation parameters. Presently, this is not an objective of the primary Cassini mission. As discussed below, assessment of hydrostatic equilibrium can also be achieved by combination of topographic and gravity measurements. Recent shape measurements for the Saturnian satellites [*Thomas et al.*, 2006] indicate that some of those bodies, especially Iapetus and Enceladus, deviate from hydrostatic equilibrium. At this stage, the uncertainty on Rhea's shape is too large ($a - c = 4.4 \pm 2.7$ km) to provide meaningful information on the density profile. However, the mean value $a - c = 4.4$ km hints at potential deviation from the value expected for hydrostatic equilibrium.

4.3. Combination With Other Cassini Observations

4.3.1. Observations by Other Cassini Instruments

[84] Cassini brings onboard instruments with the capability to collect information on the composition and thermal state of Saturn's icy satellites (see *Lunine and Soderblom* [2002] for a review of the science objectives of the different Cassini instruments at Saturn's icy satellites).

[85] Cassini Dust Analyzer (CDA) [e.g., *Srama et al.*, 2004] will determine the chemical composition of the dust by direct probing of the satellites Hill's sphere. Remote sensing of the sputtering at the surface will be performed by Cassini Plasma Spectrometer (CAPS) and Ionic and Neutral Mass Spectrometer (INMS). Combination of the images provided by the Imaging Science Subsystem (ISS), the Ultraviolet Imaging Spectrograph Subsystem, the Composite Infrared Spectrometer (CIRS) and Visual and Infrared Mapping Spectrometer Subsystem (VIMS) will provide compositional mapping of the surface unit. This may in turn help discriminate between an endogenic or exogenic origin of the surfaces state and provide constraints on the surface composition. The CIRS instrument will also provide information on thermal properties and detect regions where there has been recent or even ongoing activity, such as cryovolcanism. RADAR measurements (in its passive radiometry mode) will provide complementary information.

4.3.2. Topography Data

[86] Estimation of the dimensionless moment of inertia can also be derived from topography measurements, as explained by *Zharkov et al.* [1985], and applied for example by *Dermott and Thomas* [1991] in the case of Mimas. After *Zharkov et al.* [1985], we express the difference between the equatorial radius a and the polar radius c as

$$a - c = 2\ R\ q_t\ h_s, \tag{21}$$

where h_s is the topographic tidal Love number and q_t the tidal parameter defined in equation (20).

[87] Comparison of h_s and k_s provides information on potential departure from hydrostatic equilibrium due to large-scale topography anomalies or density anomalies. Hydrostatic equilibrium is expressed through the equality $h_s = k_s + 1$.

[88] The range of variation of (a–c) for the different models is presented in Table 5. This difference varies from 2.20 km for the models where there has been full differentiation of the rock phase from the ice (type E) to 2.86 km for undifferentiated models. This implies that determination of the radius must be performed with an accuracy better than 660 m in order to get information on the differentiation degree of the satellite. This corresponds to a relative variation of 23%, while gravity measurement, such as C_{22}, are more sensitive to the density profile, with a range of 43% between extrema values.

4.4. Refining the Geodynamical Models

[89] Apart from *Forni et al.*'s [1991] modeling of Dione's thermal evolution, and *McKinnon*'s [1998] synthesis study of the geodynamics of icy satellites, no thorough thermal evolution modeling of Saturn's small icy satellites have been produced since the mid eighties. There is a need to develop new thermal evolution models by applying the concepts developed over the past 20 years (e.g., variable viscosity, influence of ammonia, impact of the exothermic ice I-II transition, composition gradients in recent models of Saturn's subnebula evolution) that have been applied to large icy satellites [e.g., *Deschamps and Sotin*, 2001]. Also, new thermal modeling taking into account the latest thermal transfer theories (e.g., convection onset) and material properties (e.g., thermal conductivity as a function of composition and porosity) will help identify potential unrealistic models among those presented in this study. For example, this would result in a new assessment on whether ice II should be stable inside Rhea.

4.5. Comparative Planetology: The Need for More Data

[90] In order to get a global understanding of the evolution of the Saturnian medium-sized satellites, it is fundamental to get information on the gravity field of these bodies. If the degree two gravity coefficients are unable to indicate the differentiation state of Rhea, then comparison of similar measurements acquired for other satellites could help decrease the uncertainty. For example, Dione is thought by *Ellsworth and Schubert* [1983] and *Schubert et al.* [1986] to have undergone the same thermal evolution as Rhea. Iapetus has a mean radius of 735 ± 3 km, close to Rhea's radius, but a density of 1087 ± 17 kg/m^3 [*Jacobson et al.*, 2005]. Iapetus' smaller rock phase mass fraction and the consequent smaller radiogenic energy budget could have resulted in a different internal evolution with respect to Rhea, if geodynamical models proposed so far are valid. Correlation between the clues on the interior of these different satellites provided by direct measurement of their gravity field would help get the big picture on their formation and evolution, and constrain geodynamical and thermal evolution models.

5. Conclusion

[91] We have discussed the improvement of our knowledge of Rhea's interior from the direct measurement of its gravity field by Cassini radio science subsystems scheduled in November 2005. The available information allows us to design ten different models of Rhea's interior. Poor constraints on the parameters involved in the models, such as the degree of differentiation, the rock phase density and the presence or absence of ice II implies an overlap of values of C_{22} for most models.

[92] For extreme values of C_{22} it is possible to characterize the degree of differentiation of the body, as follows.

[93] 1. If C_{22} is lower than 1.90×10^{-4}, we can identify that Rhea is differentiated in a rocky core and an ice mantle. Then, C_{22} is independent on the presence or absence of ice II. There is a direct relationship between C_{22} and the core radius, which in turn yields the rock phase density (Figure 4).

[94] 2. If C_{22} is higher than 2.50×10^{-4}, we can conclude that the body is undifferentiated. This is the only case that provides the opportunity to get unambiguous information on the presence of ice II as C_{22} is then uniquely a function of the presence or absence of ice II.

[95] For values of C_{22} between 1.90×10^{-4} and 2.50×10^{-4}, models overlap. Thus it is necessary to make an assumption on the degree of differentiation of Rhea. Further assumptions can be made on the rock phase density and the presence of ice II.

[96] If we assume that Rhea's interior is described by a model of type B, and we make an assumption on the presence or absence of ice II, it is possible to estimate from C_{22} the thickness of the outer ice layer (Figure 5). If we assume that Rhea can be described as a model of type C, it is possible to deduce from C_{22} the presence or absence of ice II. Estimation of the rocky core radius requires assuming the density of the rock phase.

[97] Models of type D might be the most realistic representation of Rhea's interior. Owing to the numerous parameters involved in these models, their characterization from the inversion of degree-two gravity coefficients requires assuming both the presence or absence of ice II and the rock phase density, as well as the density of the rock-ice layer (Figure 5).

[98] The effect of potential nonhydrostatic contributions is likely to further impede the accurate interpretation of the degree-two gravity coefficients in terms of interior models. The general ideas presented in this paper apply to other icy satellites comparable to Rhea in size (likely to have internal pressure conditions suitable for ice II crystallization), such as Dione, and the large Uranian satellites.

[99] Regarding the characterization of the interior of the icy satellites, *Lupo* [1982] concluded in his study based on Voyager observations that "The wait for a reliable value of I/MR2 for any of these bodies is likely to be a long one." Fortunately, *Cassini* is there.

[100] **Acknowledgments.** This work has been realized while the author was a NRC Research Associate at the Jet Propulsion Laboratory. The author is extremely grateful to Dennis Matson for the significant improvement he made to the initial version of this document. Many thanks are owed to Torrence Johnson, Frank Sohl, Tilmann Denk, Christophe Sotin, and Jonathan Lunine, for their valuable comments and corrections. Many thanks are owed also to Lindsey Bruesch, Gerald Schubert, and Francis Nimmo, for their reviews. Their comments have contributed to increasing the clarity of this document, and their suggestion to address the critical issue of hydrostatic equilibrium has been much appreciated.

References

Anderson, J. D., R. A. Jacobson, E. L. Lau, W. B. Moore, and G. Schubert (2001), Io's gravity field and interior structure, *J. Geophys. Res.*, *106*, 32,963–32,970.

Anderson, J. D., N. J. Rappaport, G. Giampieri, G. Schubert, and W. B. Moore (2003), Gravity field and interior structure of Rhea, *Phys. Earth Planet. Inter.*, *136*, 201–213.

Anderson, J. D., G. Schubert, R. A. Jacobson, E. L. Lau, W. B. Moore, and J. L. Pagulta (2004), Discovery of mass anomalies on Ganymede, *Science*, *305*, 989–991.

Bridgman, P. (1937), The phase diagram of water to 45,000 kg/cm^3, *J. Chem. Phys.*, *5*, 964–966.

Buratti, B. J., J. A. Mosher, and T. V. Johnson (1990), Albedo and color maps of the Saturnian satellites, *Icarus*, *87*, 339–357.

Castillo, J. C., D. L. Matson, C. Sotin, T. V. Johnson, J. I. Lunine, and P. C. Thomas (2005), A geophysical study of Iapetus: The need for and consequence of ^{26}Al, *Bull. Am. Astron. Soc.*, *37*, 39.04.

Chzechowski, L., and J. Leliwa-Kopystynski (2002), Solid state convection in the icy satellites: Numerical results, *Adv. Space Res.*, *29*, 757–762.

Consolmagno, G. J. (1985), Resurfacing Saturn's satellites—Models of partial differentiation and expansion, *Icarus*, *64*, 401–413.
Consolmagno, G. J., and J. S. Lewis (1978), The evolution of icy satellites and surfaces, *Icarus*, *34*, 280–293.
Denk, T., et al. (2005), The first six months of Iapetus observations by the Cassini ISS camera, *Lunar Planet. Sci.*, *XXXVI*, abstract 2262.
Dermott, S. F., and P. C. Thomas (1991), The shape and internal structure of Mimas, *Icarus*, *73*, 25–65.
Deschamps, F., and C. Sotin (2001), Thermal convection in the outer shell of large icy satellites, *J. Geophys. Res.*, *106*, 5107–5121.
Durham, W. B., and L. A. Stern (2001), Rheological properties of water ice-applications to satellites of the outer planets, *Annu. Rev. Earth Planet. Sci.*, *29*, 295–330.
Ellsworth, K., and G. Schubert (1983), Saturn's icy satellites—Thermal and structural models, *Icarus*, *54*, 490–510.
Federico, C., and P. Lanciano (1983), Thermal and structural evolution of four satellites of Saturn, *Ann. Geophys.*, *1*, 469–476.
Forni, O., A. Coradini, and C. Federico (1991), Convection and lithospheric strength in Dione, an icy satellite of Saturn, *Icarus*, *94*, 232–245.
Fortes, A. D., I. G. Wood, J. P. Brodholt, and L. Vocadlo (2003), Ab initio simulation of the ice II structure, *J. Chem. Phys.*, *119*, 4567–4572.
Gagnon, R. E., H. Kiefte, M. J. Clouter, and E. Whalley (1990), Acoustic velocities and densities of polycrystalline ice Ih, II, III, V and VI by Brillouin spectroscopy, *J. Chem. Phys*, *92*, 1909–1914.
Hogenboom, D. L., J. S. Kargel, G. J. Consolmagno, T. C. Holden, L. Lee, and M. Buyyounouski (1997), The ammonia-water system and the chemical differentiation of icy satellites, *Icarus*, *128*, 171–180.
Jacobson, R. A., et al. (2005), The gravity field of the Saturnian system and the orbits of the major Saturnian satellites, *Bull. Am. Astron. Soc.*, *37*, 47.11.
Kargel, S. J. (1998), Physical chemistry of ices in the outer solar system, in *Solar System Ices*, *Astrophys. Space Sci. Libr.*, vol. 227, pp. 2–25, Springer, New York.
Kaula, W. M. (1966), *Theory of Satellite Geodesy*, 124 pp. Blaisdell, Waltham, Mass.
Leliwa-Kopystynski, J., and K. J. Kossacki (2000), Evolution of porosity in small icy bodies, *Planet. Space Sci.*, *48*, 727–745.
Lunine, J., and L. Soderblom (2002), Cassini-Huygens investigations of satellite surfaces and interiors, *Space Sci. Rev.*, *104*, 191–208.
Lupo, M. J. (1982), Mass-radius relationships in icy satellites after Voyager, *Icarus*, *52*, 40–53.
Lupo, M. J., and J. S. Lewis (1979), Mass-radius relationships in icy satellites, *Icarus*, *40*, 157–170.
Matson, D. L., L. J. Spilker, and J.-P. Lebreton (2002), The Cassini/Huygens mission to the Saturnian system, *Space Sci. Rev.*, *104*, 1–58.
McKinnon, W. (1998), Geodynamics of icy satellites, in *Solar System Ices*, *Astrophys. Space Sci. Libr.*, vol. 227, pp. 525–533, Springer, New York.
McKinnon, W. B., and S. Desai (2003), Internal structures of the Galilean satellites: What can we really tell?, *Bull. Am. Astron. Soc.*, *34*, 2104.
Morrison, D., T. Owen, and L. A. Soderblom (1986), The satellites of Saturn, in *Satellites*, pp. 764–801, Univ. of Ariz. Press, Tucson.
Mueller, S., and W. B. McKinnon (1988), Three-layered models of Ganymede and Callisto— Compositions, structures, and aspects of evolution, *Icarus*, *76*, 437–464.
Palguta, J., J. D. Anderson, G. Schubert, and W. B. Moore (2004), Mass anomalies on Ganymede, *Eos Trans. AGU*, *85*(47), Fall Meet. Suppl., Abstract P31A-0967.
Petrenko, V. F., and R. W. Whitworth (1999), The other phases of ice, in *Physics of Ice*, pp. 252–283, Clarendon Press, Oxford, U. K.
Prialnik, D., and A. Bar-Nun (1990), Heating and melting of small icy satellites by the decay of ^{26}Al, *Astrophys. J.*, *355*, 281–286.
Rainey, E. S., and D. J. Stevenson (2003), Oceans in ice-rock bodies: Conditions for the existence of subsurface liquid water, *Eos Trans. AGU*, *84*(46), Fall Meet. Suppl., Abstract P51B-0447.
Schubert, G., T. Spohn, and R. T. Reynolds (1986), Thermal histories, compositions and internal structures of the moons of the Solar System, in *Satellites*, pp. 224–292, Univ. of Ariz. Press, Tucson.
Scott, H. P., Q. Williams, and F. J. Ryerson (2002), Experimental constraints on the chemical evolution of large icy satellites, *Earth Planet. Sci. Lett.*, *203*, 399–412.
Srama, R., et al. (2004), The Cassini cosmic dust analyzer, *Space Sci. Rev.*, *114*, 465–518.
Stevenson, D. (1982), Volcanism and igneous processes in small icy satellites, *Nature*, *298*, 142–144.
Thomas, P. G. (1988), The tectonic and volcanic history of Rhea as inferred from studies of scarps, ridges, troughs, and other lineaments, *Icarus*, *74*, 554–567.
Thomas, P. C., J. Veverka, P. Helfenstein, C. Porco, J. Burns, T. Denk, E. Turtle, R. A. Jacobson, and the ISS Science team (2006), Shapes of the Saturnian Icy Satellites, *Lunar Planet. Sci.*, *XXXVII*, abstract 1639.
Verbiscer, A. J., and J. Verveka (1989), Albedo dichotomy of Rhea: Hapke analysis of Voyager photometry, *Icarus*, *82*, 336–353.
Yoder, C. F. (1995), Astrometric and geodetic properties of the Earth and the Solar System, in *Global Earth Physics: A Handbook of Physical Constants*, *AGU Ref. Shelf*, vol. 1, edited by T. J. Ahrens, pp. 1–31, AGU, Washington, D. C.
Zharkov, V. N., V. V. Leontjev, and A. V. Kozenko (1985), Models, figures, and gravitational moments of the Galilean satellites of Jupiter and icy satellites of Saturn, *Icarus*, *61*, 92–100.
Zolotov, M. Y., E. L. Shock, and W. B. McKinnon (2002), Effects of early water-rock chemical interactions on interior structures, physical properties, and heat balances of Galilean satellites, *Eos Trans. AGU*, *83*(47), Fall Meet. Suppl., abstract P72B-0498.

J. Castillo-Rogez, Jet Propulsion Laboratory, California Institute of Technology, M/S 230-260V, 4800 Oak Grove Drive, Pasadena, CA 91109, USA. (julie.c.castillo@jpl.nasa.gov)